

Chapter 6

Mapping photonic entanglement into and out of quantum memories

This chapter is largely based on ref.³⁰. Reference³⁰ refers to the then current literature in 2008 at the time of publication.

6.1 Introduction

In the quest to achieve quantum networks over long distances^{1,227}, an area of considerable activity has been the interaction of light with atomic ensembles comprised of a large collection of identical atoms (ref.⁴, see also chapter 1). In the regime of continuous variables, a particularly notable advance has been the teleportation of quantum states between light and matter⁶⁰. For discrete variables with photons taken one by one, important achievements include the efficient mapping of collective atomic excitations to single photons (refs.^{76,77,79,80}, chapter 2), the realization of entanglement between distant ensembles (refs.^{27,34}, chapter 3) and, recently, entanglement distribution involving two pairs of ensembles (ref.³⁶, chapter 4). The first step toward entanglement swapping has been made (ref.³⁷, chapter 5), and light-matter teleportation has been demonstrated with post-diction¹¹².

In all these cases, progress with single photons has relied upon probabilistic schemes following the measurement-induced approach developed in the seminal paper by Duan, Lukin, Cirac and Zoller (*DLCZ*)⁴ and subsequent extensions⁴⁹. For the *DLCZ* protocol, heralded entanglement is generated by detecting a single photon emitted indistinguishably by one of two ensembles. Intrinsically, the probability p to prepare entanglement with only 1 excitation shared between two ensembles is related to the quality of entanglement, since the likelihood for contamination of the entangled state by processes involving 2 excitations likewise scales as p (ref.³⁴, chapter 3), and results in low success probability. Although the degree of stored entanglement can approach unity for the (rare) successful trials (ref.³⁴, chapter 3), the condition $p \ll 1$ dictates reductions in the count rate and compromises in the quality of the resulting entangled state (e.g., as $p \rightarrow 0$, processes such as stray light scattering and detector dark counts become increasingly important). Further-

more, for finite memory time, subsequent connection of entanglement becomes increasingly challenging (ref.³⁷, chapter 5).

The separation of processes for the generation of entanglement and for its storage enables this drawback to be overcome. In this chapter, we demonstrate such a division by way of reversible mapping of an entangled state into a quantum memory. The mapping is obtained by using adiabatic passage based upon dynamic electromagnetically induced transparency (EIT) (refs.^{86,88,89,94}, see also sections 2.5 and 6.9 for details). Storage and retrieval of optical pulses have been demonstrated previously, for both classical pulses^{90,91} and single-photon pulses^{92,93}. Adiabatic transfer of a collective excitation has been demonstrated between two ensembles coupled by a cavity mode²⁹, which can provide a suitable approach for generating on-demand entanglement over short distances. However, for efficient distribution of entanglement over quantum networks, reversible mapping of an entangled state between matter and light, as illustrated in Fig. 6.1a, has not been addressed until now.

In our experiment, entanglement between two atomic ensembles L_a, R_a is created by first splitting a single photon into two modes L_{in}, R_{in} to generate an entangled state of light^{228–230}. This entangled field state is then coherently mapped to an entangled matter state for L_a, R_a . On demand, the stored atomic entanglement for L_a, R_a is converted back into entangled photonic modes L_{out}, R_{out} . As opposed to the original *DLCZ* scheme, our approach is inherently deterministic, suffering principally from the finite efficiency of mapping single excitations to and from an atomic memory, with efficiency $\simeq 50\%$ having been achieved. Moreover, the contamination of entanglement for L_a, R_a from processes involving 2 excitations can be arbitrarily suppressed (independent of the mapping probabilities) with continuing advances in on-demand single-photon sources²³¹. Our experiment thereby provides a promising avenue to distribute and store quantum entanglement deterministically over remote atomic ensembles for scalable quantum networks²³² (see also chapter 10 for a potential application of this scheme for hybrid quantum networks).

6.2 Deterministic quantum interface between matter and light

The experimental setup is depicted in Fig. 6.1. Our single-photon source is based on Raman transitions in an optically thick cesium ensemble^{4,76}, called a source ensemble (see section 6.8). This system generates 28-ns-long single photons (resonant with $6S_{1/2}, F = 4 \leftrightarrow 6P_{3/2}, F' = 4$ transition) in a heralded fashion⁷⁶. The single photons are polarized at 45° from the eigen-polarizations of the beam displacer BD_1 (Fig. 1b) which splits them into entangled optical modes L_{in}, R_{in} (called the signal modes) to produce, in the ideal case, the following state

$$\frac{1}{\sqrt{2}}(|0_{L_{in}}\rangle|1_{R_{in}}\rangle + e^{i\phi_{in}}|1_{L_{in}}\rangle|0_{R_{in}}\rangle). \quad (6.1)$$

The next stage consists of coherently mapping the photonic entanglement for L_{in}, R_{in} into atomic ensembles L_a, R_a (called the memory ensembles) within a single cloud of cold cesium atoms in a magneto-optical

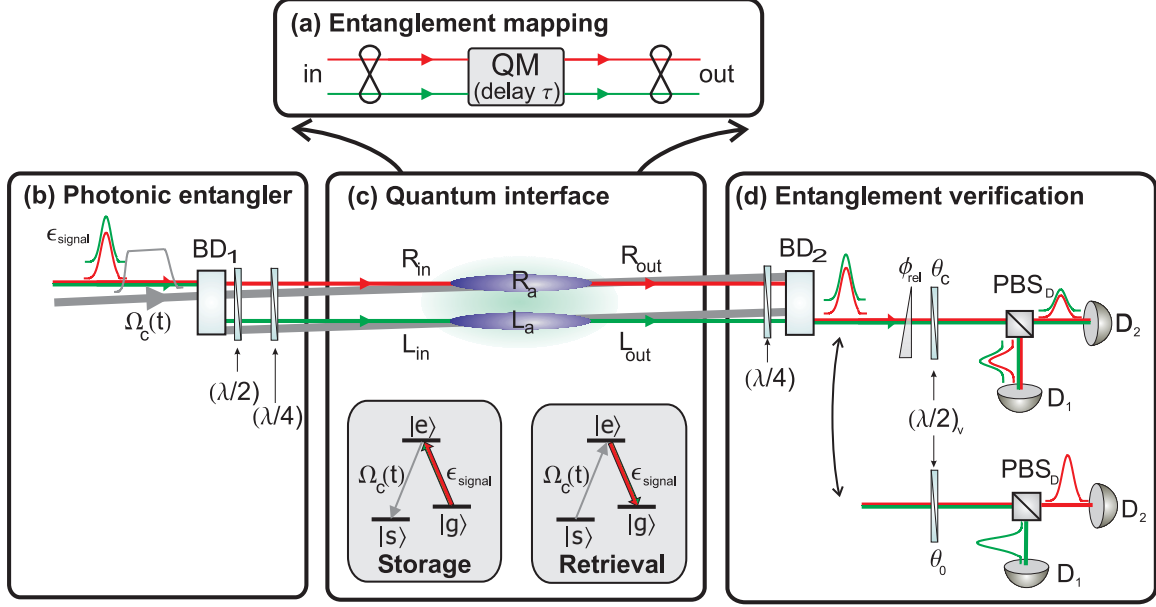


Figure 6.1: **Overview of the experiment.** **a**, Reversible mapping. Illustration of the mapping of an entangled state of light into and out of a quantum memory (QM) with controllable storage time τ . **b**, Photonic “entangler.” A beam displacer BD_1 splits an input single photon into two orthogonally polarized, entangled modes L_{in}, R_{in} , which are spatially separated by 1 mm. With waveplates $\lambda/2$ and $\lambda/4$, the signal fields ϵ_{signal} for L_{in}, R_{in} and control fields $\Omega_c^{(L,R)}(t)$ are transformed to circular polarizations with the same helicity along each path L, R , and copropagate with an angle of 3° . **c**, Quantum interface for reversible mapping. Photonic entanglement between L_{in}, R_{in} is coherently mapped into the memory ensembles L_a, R_a by switching $\Omega_c^{(L,R)}(t)$ off adiabatically. After a programmable storage time, the atomic entanglement is reversibly mapped back into optical modes L_{out}, R_{out} by switching $\Omega_c^{(L,R)}(t)$ on. Relevant energy diagrams for the storage and retrieval processes are shown in the insets. States $|g\rangle, |s\rangle$ are the hyperfine ground states $F = 4, F = 3$ of $6S_{1/2}$ in atomic cesium; state $|e\rangle$ is the hyperfine level $F' = 4$ of the electronic excited state $6P_{3/2}$. **d**, Entanglement verification. After a $\lambda/4$ plate, the beam displacer BD_2 combines modes L_{out}, R_{out} into one beam with orthogonal polarizations. With $(\lambda/2)_v$ at $\theta_c = 22.5^\circ$ before the polarization beamsplitter (PBS_D), single photon interference is recorded at detectors D_1, D_2 by varying the relative phase ϕ_{rel} by a Berek compensator. With $(\lambda/2)_v$ at $\theta_0 = 0^\circ$, photon statistics for each mode L_{out}, R_{out} are measured independently.

trap (MOT) (Fig. 6.1c). Ensembles L_a, R_a are defined by the well-separated optical paths of the entangled photonic modes L_{in}, R_{in} (section 6.6). To avoid dissipative absorption for the fields in modes L_{in}, R_{in} for our choice of polarization⁹³, we spin-polarize the atomic ensemble into a clock state $|F = 4, m_F = 0\rangle$ (section 6.6). Initially, the strong control fields $\Omega_c^{(L,R)}$ (resonant with $6S_{1/2}, F = 3 \leftrightarrow 6P_{3/2}, F' = 4$ transition) open transparency windows $\Omega_c^{(L,R)}(0)$ in L_a, R_a for the signal modes. As the wavepacket of the signal field propagates through each ensemble, the control fields $\Omega_c^{(L,R)}(t)$ are turned off in 20 ns by an electro-optical intensity modulator, thereby coherently transforming the fields of the respective signal modes to collective atomic excitations within L_a, R_a . This mapping leads to an entanglement between quantum memories L_a, R_a , with atomic state $\frac{1}{\sqrt{2}}(|\bar{g}_{L_a}\rangle|\bar{s}_{R_a}\rangle + e^{i\phi_a}|\bar{s}_{L_a}\rangle|\bar{g}_{R_a}\rangle)$. After a user-defined delay, chosen here to be $1.1 \mu\text{s}$, the atomic entanglement is converted back into entangled photonic modes by switching on the control fields $\Omega_c^{(L,R)}(t)$ (section 6.9), with a photon state $\frac{1}{\sqrt{2}}(|0_{L_{out}}\rangle|1_{R_{out}}\rangle + e^{i\phi_{out}}|1_{L_{out}}\rangle|0_{R_{out}}\rangle)$. The con-

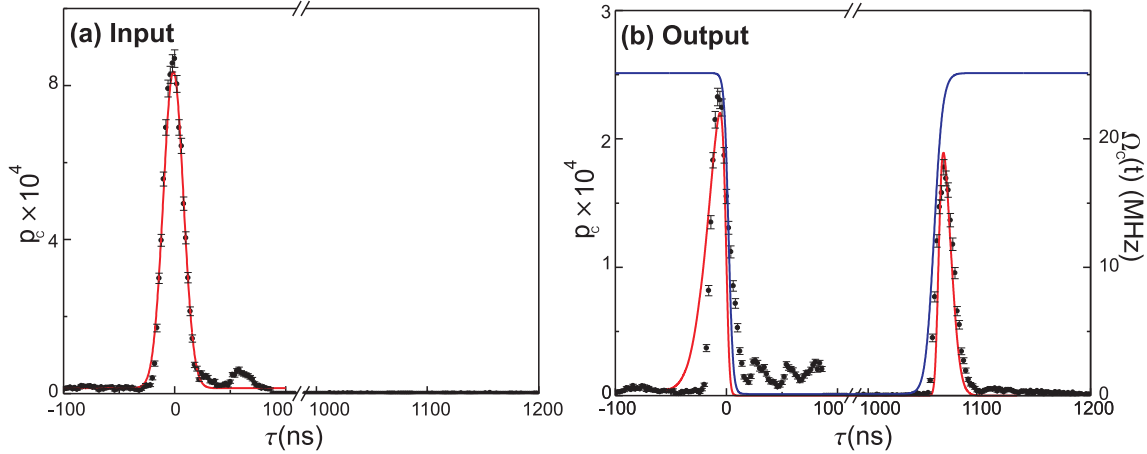


Figure 6.2: **Single-photon storage and retrieval for a single ensemble.** **a**, Input. The data points are the measured probability p_c for the signal field, a single photon generated from a separate “offline” source atomic ensemble⁷⁶. The red solid line represents a Gaussian fit of $1/e$ width of 28 ns. **b**, Storage and retrieval. The points around $\tau = 0 \mu\text{s}$ represent “leakage” of the signal field due to the finite optical depth and length of the ensemble. The points beyond $\tau = 1 \mu\text{s}$ show the retrieved signal field. The overall storage and retrieval efficiency is $17 \pm 1 \%$. The blue solid line is the estimated Rabi frequency $\Omega_c(t)$ of the control pulse. The red solid curve is from a numerical calculation solving the equation of motion of the signal field in a dressed medium (ref.⁸⁶, chapter 2). Error bars give the statistical error for each point.

trolled readout allows the extensions to quantum controls for entanglement connection and distribution by way of asynchronous preparation (refs.^{36,37}, chapters 4 and 5).

6.2.1 Single-photon storage and retrieval

For a given optical depth \tilde{d}_0 , there is an optimal Rabi frequency $\Omega_c(t)$ for the control field. In our experiment, \tilde{d}_0 and $\Omega_c(0)$ are 15 and 24 MHz, respectively. An example of our measurements of the EIT process for a single ensemble is presented in Fig. 6.2, which shows the input single-photon pulse (Fig. 6.2a) and its storage and retrieval (Fig. 6.2b); see also chapter 2. Due to finite \tilde{d}_0 , small length (≈ 3 mm) of the ensemble and the turn-off time of the intensity modulator, there is considerable loss in the storage process, as evidenced by the counts around $\tau = 0 \mu\text{s}$ in Fig. 6.2b. The peak beyond $\tau = 1 \mu\text{s}$ represents the retrieved pulse after $1.1 \mu\text{s}$ of storage. Overall, we find good agreement between our measurements and the numerical calculation following the methods of ref.⁸⁶, using the fitted function of the input signal field (Fig. 6.2a) as the initial condition, with all other parameters from independent measurements (section 6.9). We find the overall storage and retrieval efficiency of $\eta_{\text{sr}} = 17 \pm 1 \%$, also in agreement with the simulation of $\eta_{\text{sr}}^{\text{theory}} = 18 \%$.

6.2.2 Entanglement verification

With these results in hand for the individual L_a, R_a ensembles, we next turn to the question of verification of entanglement for the optical modes of $L_{\text{in}}, R_{\text{in}}$ and $L_{\text{out}}, R_{\text{out}}$. We follow the protocol introduced in ref.²⁷

by (1) reconstructing a reduced density matrix $\hat{\rho}$ constrained to a subspace containing no more than one excitation in each mode, and (2) assuming that all off-diagonal elements between states with different numbers of photons vanish, thereby obtaining a lower bound for any purported entanglement. In the photon-number basis $|n_L, m_R\rangle$ with $\{n, m\} = \{0, 1\}$, the reduced density matrix $\hat{\rho}$ is written as (ref.²⁷, chapter 3)

$$\hat{\rho} = \frac{1}{P} \begin{pmatrix} p_{00} & 0 & 0 & 0 \\ 0 & p_{10} & d & 0 \\ 0 & d^* & p_{01} & 0 \\ 0 & 0 & 0 & p_{11} \end{pmatrix}. \quad (6.2)$$

Here, p_{ij} is the probability to find i photons in mode L_k and j in mode R_k , $d \simeq \frac{V(p_{10}+p_{01})}{2}$ is the coherence between $|1_L 0_R\rangle_k$ and $|0_L 1_R\rangle_k$, $P = p_{00} + p_{10} + p_{01} + p_{11}$, and V is the visibility for interference between modes L_k, R_k , with $k \in \{\text{in}, \text{out}\}$. The degree of entanglement of $\hat{\rho}$ can be quantified in terms of concurrence, $C = \frac{1}{P} \max(0, 2|d| - 2\sqrt{p_{00}p_{11}})$, which is a monotone function of entanglement, ranging from 0 for a separable state to 1 for a maximally entangled state¹⁷⁸.

6.3 Coherent and reversible quantum interface for photonic entanglement

6.3.1 Quantum-state tomography on the input photonic state

We first perform tomography on the input modes $L_{\text{in}}, R_{\text{in}}$ to verify that they are indeed entangled. To this end, we remove the memory ensembles to transmit directly the signal fields into the verification stage, following our protocol of complementary measurements as described in Fig. 6.1d (See section 6.7). The interference fringes between the two input modes are shown in Fig. 6.3a. From the independently determined propagation and detection efficiencies, we use the measurements at D_1, D_2 to infer the quantum state for the input modes $L_{\text{in}}, R_{\text{in}}$ entering the faces of L_a, R_a , with the reconstructed density matrix $\hat{\rho}_{\text{in}}$ given in Fig. 6.3a. The concurrence derived from $\hat{\rho}_{\text{in}}$ is $C_{\text{in}} = 0.10 \pm 0.02$, so that the fields for $L_{\text{in}}, R_{\text{in}}$ are indeed entangled. The value of the concurrence is in good agreement with the independently derived expectation of $C_{\text{in}}^{\text{theory}} = 0.10 \pm 0.01$, which depends on the quality of the single photon and the vacuum component (i.e., the overall efficiency) (ref.³⁴, chapter 3). Given a heralding click from our single-photon source, the probability to have a single photon at the face of either memory ensemble is 15 %, leading to a vacuum component of 85 %. We also independently characterize the suppression w of the two-photon component relative to a coherent state (for which $w = 1$) and find $w = 0.09 \pm 0.03$. Our input entanglement is only limited by the current properties of our single-photon source, which will be improved with the rapid advances in sources of single photons²³¹.

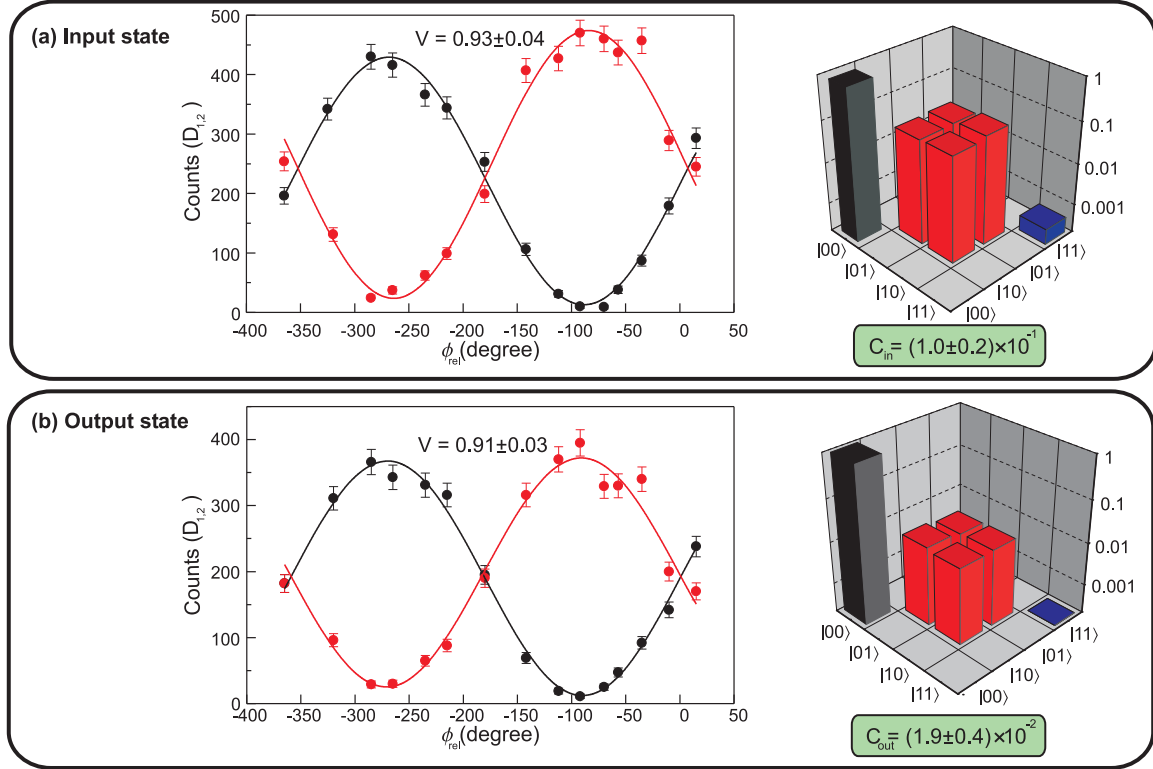


Figure 6.3: **Entanglement for the input and output optical modes.** To verify entanglement, complementary measurements are performed : interference leading to a fringe when the relative phase ϕ_{rel} is scanned and independent photon statistics for each light mode. The figure shows the interference fringes and the reconstructed density matrices (in log scale) for the photonic modes **a**, at the input of the memory and **b**, the output after storage and retrieval. The estimated concurrence is given in each case. Each point of the fringe is taken for 20, 000 (100, 000) heralding events for the input (output) state. Error bars indicate statistical errors.

6.3.2 Quantum-state tomography on the output photonic state

Having verified the entanglement for the input modes $L_{\text{in}}, R_{\text{in}}$, we next map this photonic entanglement into $L_{\text{a}}, R_{\text{a}}$, which serve as a quantum memory (Fig. 6.1c). After storing the entanglement for $1.1 \mu\text{s}$, we transfer the resulting atomic excitation on demand from the memory to the output modes $L_{\text{out}}, R_{\text{out}}$ and perform quantum-state tomography to determine $\hat{\rho}_{\text{out}}$ as for $\hat{\rho}_{\text{in}}$. As shown in Fig. 6.3, the visibility for interference of the fields after storage and retrieval shows no appreciable degradation (from $V_{\text{in}} = 0.93 \pm 0.04$ to $V_{\text{out}} = 0.91 \pm 0.03$). From the measurements at D_1, D_2 , we infer the quantum state $\hat{\rho}_{\text{out}}$ at the output faces of $L_{\text{a}}, R_{\text{a}}$, as displayed in Fig. 6.3b. The associated concurrence $C_{\text{out}} = (1.9 \pm 0.4) \times 10^{-2}$ is in agreement with $C_{\text{out}}^{\text{theory}} = (1.7 \pm 0.1) \times 10^{-2}$. Since mapping of atomic states from $L_{\text{a}}, R_{\text{a}}$ into field modes $L_{\text{out}}, R_{\text{out}}$ is a local operation, this measurement provides a lower bound for the entanglement between the $L_{\text{a}}, R_{\text{a}}$ ensembles. Thus, we demonstrate the reversible mapping of an entangled state of the electromagnetic field to and from a material system. For completeness, Table 6.1 gives the diagonal elements and concurrences of $\hat{\rho}_{\text{in}}, \hat{\rho}_{\text{out}}$ determined directly at D_1, D_2 without correction for propagation and detection efficiencies.

6.4 Discussion and analysis

We emphasize that although the entanglement associated with $\hat{\rho}_{\text{out}}$ is heralded (because of the nature of our single-photon source), our protocol for generation and storage of entanglement is intrinsically deterministic. The transfer efficiency of entanglement from input modes to output modes of the quantum memory is limited by the storage and retrieval efficiency η_{sr} of the EIT process. This transfer can be quantified by the ratio $\tilde{\lambda}$ of the concurrence C_{out} for the output state $\hat{\rho}_{\text{out}}$ to C_{in} for the input state $\hat{\rho}_{\text{in}}$. For an ideal source of single photons on-demand (with no vacuum component), the input concurrence is approximated by $C_{\text{in}} \simeq \alpha V$, where α denotes the transmission efficiency of the single photon from the source to the entangler in Fig. 6.1b (ref.³⁴, chapter 3). Similarly, for the output, $C_{\text{out}} \simeq \alpha \eta_{\text{sr}} V$, where we assume that the visibility V is preserved by the mapping processes. Thus, $\tilde{\lambda} = \frac{C_{\text{out}}}{C_{\text{in}}} \simeq \eta_{\text{sr}}$, which therefore estimates the maximum amount of entanglement in modes $L_{\text{out}}, R_{\text{out}}$ for the case of an (ideal) single photon generated deterministically. In our experiment, the entanglement transfer reaches $\tilde{\lambda} = (20 \pm 5) \%$. By way of optimal pulse shaping and improved optical depth, the entanglement transfer can be greatly improved (section 6.10.2).

The performance of our quantum interface depends also on the memory time τ_{m} over which one can faithfully retrieve a stored quantum state. For our system, independent measurements of η_{r} made by varying the storage duration τ allow us to determine $\tau_{\text{m}} = 8 \pm 1 \mu\text{s}$, as limited by inhomogeneous Zeeman broadening and motional dephasing (section 6.6 and chapter 2). Active and passive compensations of the residual magnetic field would improve τ_{m} , along with improved optical trapping techniques (chapter 2).

6.5 Conclusion

In conclusion, our work provides the first realization of mapping an entangled state into and out of a quantum memory. Our protocol alleviates the significant drawback of probabilistic protocols⁴, where low preparation probabilities prevent its potential scalability³⁷, and thus our strategy leads to efficient scaling for high-fidelity quantum communication²³². Our current results are limited by the large vacuum component of our available single-photon source, which principally reduces the degree of entanglement in the input, and by the limited retrieval efficiency of the EIT process, which bounds the entanglement transfer to $\tilde{\lambda} = (20 \pm 5) \%$. With improved retrieval efficiency and memory time, along with the rapid development of on-demand

Table 6.1: **Experimentally determined diagonal elements and concurrences.** We directly measure the diagonal elements \bar{p}_{ij} and concurrences $\bar{C}_{\text{in}}, \bar{C}_{\text{out}}$ for the density matrices $\hat{\rho}_{\text{in}}, \hat{\rho}_{\text{out}}$ derived directly from detectors D_1, D_2 without correction for losses and detection efficiencies. Statistical errors are also given.

| | $\hat{\rho}_{\text{in}}$ | $\hat{\rho}_{\text{out}}$ |
|----------------|------------------------------------|----------------------------------|
| \bar{p}_{00} | 0.9800 ± 0.0001 | 0.99625 ± 0.00003 |
| \bar{p}_{10} | $(1.043 \pm 0.008) \times 10^{-2}$ | $(2.09 \pm 0.02) \times 10^{-3}$ |
| \bar{p}_{01} | $(0.957 \pm 0.008) \times 10^{-2}$ | $(1.67 \pm 0.02) \times 10^{-3}$ |
| \bar{p}_{11} | $(8 \pm 2) \times 10^{-6}$ | $(2 \pm 2) \times 10^{-7}$ |
| \bar{C} | $(1.28 \pm 0.09) \times 10^{-2}$ | $(2.5 \pm 0.5) \times 10^{-3}$ |

single-photon sources²³¹, our protocol enables the deterministic generation, storage, and distribution of entanglement among remote quantum memories for scalable quantum networks. Such networks have diverse applications in quantum information science, including for quantum metrology, where quantum sensing is provided by the atomic entanglement and readout by coherent mapping to the photonic modes (chapter 9).

In the broader context of quantum information theory, our experiment provides an important contribution to the lively debate about “*single-particle*” entanglement^{228,229,233}. One resolution of these discussions is a gedanken experiment in which an entangled state for a single-particle is mapped into a two-particle system by local operations, thereby verifying the presence of entanglement for the original “*single-particle*” state²³³. Our experiment demonstrates that an entangled state with one photonic excitation shared between two optical modes (see Eq. 6.1) can be converted into an entangled state for two atomic ensembles by way of coherent mapping. The presence of entanglement between the two atomic ensembles is explicitly quantified by the lower bound $C_{\text{out}} = (1.9 \pm 0.4) \times 10^{-2}$, thereby realizing the proposal of ref.²³³ for “*single-particle*” entanglement.

6.6 Experimental details

A 22 ms preparation stage and 3 ms experiment run are conducted every 25 ms period. During the preparation stage, atomic ensembles are loaded in a MOT for 18 ms and further cooled by optical molasses for 3 ms where the MOT magnetic field is turned off. For 800 μs , we optically pump the atomic ensembles to the $6S_{1/2} |F = 4, m_F = 0\rangle$ state in atomic cesium. During this stage, the trapping beam is turned off while the intensity of the repumping beam is reduced to $0.1I_{\text{sat}}$ where I_{sat} is the saturation intensity. The quantization axis is chosen along the k -vector of the signal modes and defined by a pulsed magnetic field of 0.2 G. A pair of counter-propagating Zeeman pumping beams (10 MHz red-detuned from $4 \leftrightarrow 4'$ transition and linearly polarized along the quantization axis) illuminate the ensembles in a direction perpendicular to modes $L_{\text{in}}, R_{\text{in}}$. The MOT repumping beam serves as a hyperfine pumping beam. The experiment is conducted at a repetition rate of 1.7 MHz during a 3 ms interval before the next MOT loading cycle. A small bias field of 10 mG is left on to define the quantization axis for the experiment. The various photon statistics throughout the experiment are detected by single-photon Si-avalanche Photodetectors (Perkin-Elmer SPCM-AQR-13) where the pulse signals are stamped with 2 ns resolution into a file by a 4-channel event time digitizer (FAST ComTec P7888) for data-acquisition. The overall transmission efficiencies (including the detector and propagation efficiencies) are $12 \pm 2\%$ and $14 \pm 2\%$ for the ensembles $L_{\text{a}}, R_{\text{a}}$.

The limitations to our experiment imposed by inhomogeneous Zeeman broadening are described in ref.³⁴ (chapters 2–3). Possible misalignment between the quantization axis and the bias magnetic field is estimated to be below 5 degrees. Following ref.¹⁹⁵, we are investigating active compensation of the residual magnetic field to improve τ_{m} . In our experiment, the memory time τ_{m} was also plagued by the residual control laser during storage due to finite extinction ratio 50 dB of the modulator (waveguide electro-optical modulator and

two sets of acousto-optical modulators), which set $\tau_m \simeq 1$ ms. In addition, thermal motion of the atoms (at $T_d = 150$ μ K) sets the memory time of $\tau_m \simeq 15$ μ s due to the motional dephasing, where optical trapping may dramatically improve the coherence time for the collective excitations (chapter 2).

6.7 Operational verification of entanglement

Operationally, the various elements of $\hat{\rho}$ are obtained by recombining the L_k, R_k fields with a second beam displacer, BD_2 , as illustrated in Fig. 6.1d, to obtain a single spatial mode with orthogonal polarizations for the L_k, R_k fields (refs. ^{34,36}, chapters 3 and 4), with $k \in \{\text{in, out}\}$. The diagonal elements of $\hat{\rho}$ are measured with $(\lambda/2)_v$ set at 0° so that detection events at D_1, D_2 are recorded directly for the L_k, R_k fields. To determine the off-diagonal components of $\hat{\rho}$, the modes L_k, R_k are brought into interference with $(\lambda/2)_v$ set at 22.5° , as shown in Fig. 6.1d. By varying the relative phase ϕ_{rel} between the modes, we determine the visibility for single-photon interference and thereby deduce d .

6.8 Single-photon generation

The single-photon source is based upon the protocol^{4,76} composed of time-delayed photon pairs, called fields 1,2 emitted from a cesium ensemble in a MOT called the source ensemble. The source ensemble is located 3 m from the memory ensembles, both of which are synchronized by a 80 MHz clock signal. For photon-pair production, a sequence of write and read pulses illuminates the source ensemble. The single photon generation is heralded by probabilistic detection of a Raman scattered field 1 from a write pulse (10 MHz red-detuned from $4 \leftrightarrow 4'$ transition). Conditioned on the heralding signal, a strong read pulse (resonant to $3 \leftrightarrow 4'$ transition) maps the excitation into a photonic mode, field 2, with probability of 50 %, which then propagates to the setup described in Fig. 6.1. The resulting conditional probability to have a single photon, field 2, at the face of memory ensemble is 15 %. The separation between the entangled optical modes $L_{\text{in}}, R_{\text{in}}$ after the entangler is 1 mm and each of the modes is focused down to a $1/e$ full width of 50 μ m at L_a, R_a . The heralding signal triggers a control logic which disables the single-photon source and all associated laser beams for the programmable duration of the storage process for the quantum interface (ref. ³⁶, chapter 4). As the retrieval process is in the slow-light regime, the temporal shape of the single photon is controlled by the intensity of the read laser, thereby changing the group velocity of the field 2 in the source ensemble^{75,234}.

6.9 EIT storage and retrieval

The coherent interface between the signal modes and collective spin waves is achieved by dynamically controlling the EIT window $\Omega_c(t)$, defined by the atom-light interaction of a resonant control field. A quantum field propagating through an externally controlled dressed state medium is best described as a slow-light,

dark-state polariton (DSP), $\hat{\Psi}(z, t)$ ⁸⁶, a coherent mixture of matter-like and photonic excitations, expressed as (chapter 2)

$$\hat{\Psi}(z, t) = \cos \theta(t) \hat{\varepsilon}_{\text{signal}} - \sin \theta(t) \sqrt{N_A} \hat{\sigma}_{\text{gs}} \quad (6.3)$$

where $\cos^2 \theta(t) = \frac{\Omega_c^2(t)}{\Omega_c^2(t) + g_d^2 N_A} = \frac{v_g(t)}{c}$, g_d is the atom-photon coupling constant for the signal field, N_A is the number of atoms, $\hat{\sigma}_{\text{gs}}$ is the atomic coherence operator for ground states $|g\rangle$ and $|s\rangle$, and $\Omega_c(t)$ is the Rabi frequency of control field. As the signal field propagates through the medium, the group velocity v_g of the DSP is adiabatically reduced to zero as $\Omega_c(t)$ decreases to zero, thereby rotating the mixing angle $\theta(t)$ from a purely photonic state to a matter-like collective spin coherence (chapter 2). When the control field is re-activated, the collective spin excitation is coherently converted into a photonic mode in a time-reversal fashion. In the experiment, under the assumption of perfect state preparation, the relevant energy diagrams for the storage and retrieval processes are ground states $|g\rangle = |F = 4, m_F = 0\rangle$, $|s\rangle = |F = 3, m_F = 0\rangle$, and the excited state $|e\rangle = |F' = 4, m_{F'} = \pm 1\rangle$ as shown in the insets of Fig. 6.1.

The overall efficiency η_{sr} of the EIT process and the temporal shape of the output fields are predicted by numerically solving the equations of motion in ref.⁸⁶ (see chapter 2 for detailed description, see also section 6.10). Under experimental conditions, the projected storage and retrieval efficiency is $\eta_{\text{sr}}^{\text{theory}} = 18\%$ as shown in Fig. 6.2. We consider two strategies that could improve η_{sr} : increasing the optical depth and appropriate pulse-shaping. By following the same calculation as above, we find that the EIT efficiency reaches its asymptotic value of $\eta_{\text{sr}} \simeq 30\%$ when the optical depth is increased to $\tilde{d}_0 \simeq 50$ with all other parameters corresponding to the current experiment (section 6.10.2.1). On the other hand, as demonstrated in ref.²³⁵, by iterating time-reversed version of the output signal field into the input, one achieves an optimal pulse-shape for the signal field which balances the transmission loss due to finite bandwidth of the pulse and the leakage due to the imperfect compression of the signal field within the atomic ensembles to reach maximum η_{sr} for a given control field $\Omega_c(t)$. This maximum η_{sr} for a given control field is in principle only dependent on the optical depth \tilde{d}_0 (section 6.10.2.2). Equivalently, the control field $\Omega_c(t)$ can be optimized for a given signal field as investigated theoretically in ref.²³⁶. Note that efficiencies approaching 50% have been achieved in ref.²³⁵.

6.10 Theoretical discussions

The dynamics of laser-induced coherence of atomic states can dramatically modify the optical response of an atomic medium, leading to destructive quantum interferences between the excitation pathways^{95,96}. In this way, resonant absorption and refraction can be eliminated by way of electromagnetically induced transparency (EIT)⁹⁴. In this section, we describe a semi-classical theory of EIT. For a complete quantum theory of *dynamic* EIT, I refer to chapter 2, whereby the equations of motions for the fields and atomic variables are derived in a *self-consistent* manner. We also present our theoretical result of time-reversal optimization¹⁸⁸ for η_{sr} using our experimental parameters³⁰.

6.10.1 Static electromagnetically induced transparency

Here, we present a semi-classical theory for *static* EIT^{94,182,237,238}. While the situation for *dynamic* EIT is somewhat different, *static* EIT describes the phenomena of ultra-slow propagation of the signal field in a coherent atomic medium^{88,239}. We also examine the equivalence between the semi-classical model and the full quantum model.

6.10.1.1 Semi-classical model of EIT

Electromagnetically induced transparency can be explained semi-classically in terms of (1) Fano-like quantum interferences between the decay pathways of Autler-Townes resonances^{237,238}, and (2) “adiabatic preparation” or “optical pumping” to a dark state in the dressed state picture^{86,179–181,183,184}, as employed traditionally in coherent population trapping (CPT) and stimulated Raman adiabatic passage (STIRAP), respectively. In particular, I will adapt the latter approach (2), as the polaritonic quantum dynamics⁸⁶ described in chapter 2 can be mapped to a semi-classical adiabatic passage in the setting of dark and bright states¹⁸¹.

As in chapter 2, we consider an effective (*non-hermitian*) Hamiltonian \hat{H}_{EIT} for an atomic ensemble interacting with a weak classical signal field \mathcal{E}_s (Rabi frequency Ω_s) and a strong control laser (Rabi frequency Ω_c) in the rotating frame (following the notations introduced in section 2.5), with

$$\hat{H}_{\text{eff}} = \hat{H}_{\text{EIT}} - i\hbar\gamma_{ge}\hat{\sigma}_{ee} - i\hbar\gamma_{gs}\hat{\sigma}_{ss}, \quad (6.4)$$

where the system Hamiltonian \hat{H}_{EIT} for the EIT interaction is given by

$$\hat{H}_{\text{EIT}}/\hbar = \Delta_c\hat{\sigma}_{ee} - \delta\hat{\sigma}_{ss} - (\Omega_s\hat{\sigma}_{eg} + \Omega_c\hat{\sigma}_{es} + h.c.). \quad (6.5)$$

Δ_c is the single-photon detuning for the control laser, and δ is the two-photon detuning between the signal field and the control laser. Here, the decay channels ($-i\hbar\gamma_{ge}\hat{\sigma}_{ee}$, $-i\hbar\gamma_{gs}\hat{\sigma}_{ss}$) result in losses of atomic coherences at rates γ_{ge} and γ_{gs} . In the following discussions, I will assume a negligible ground-state dissipation $\gamma_{gs} \simeq 0$ and resonant excitation by the control laser with $\Delta_c = 0$.

For open quantum systems, quantum-state evolution by a master equation in the Lindblad form (e.g., for Eq. 6.5) is equivalent to that of a stochastic wave-function method (quantum-trajectory method) accompanied by quantum jumps^a (refs. 164–166,240,241). Assuming a wave-function of the form $|\psi(t)\rangle = c_g(t)|g\rangle + c_s(t)|s\rangle + c_e(t)|e\rangle$, the *non-hermitian* effective Hamiltonian \hat{H}_{eff} (Eq. 6.4) yields the following equations of motions (from the Schrödinger's equation),

$$\dot{c}_g = i\Omega_s^* c_e \quad (6.6)$$

$$\dot{c}_s = -(\gamma_{gs} - i\delta)c_s + i\Omega_c^* c_e \quad (6.7)$$

$$\dot{c}_e = -(\gamma_{ge} - i\delta)c_e + i\Omega_s c_g + i\Omega_c c_s. \quad (6.8)$$

Since $\Omega_s \ll \Omega_c$ and the initial state is $|\psi(0)\rangle = |g\rangle$, we assume that the probability amplitude remains in $c_g(t) \simeq 1$ for all time t . Fourier transforming Eqs. 6.7–6.8 (with $\partial_t \mapsto iw$) and solving for $\{c_s, c_e\}$, we obtain

$$c_s(w) = \frac{\Omega_s \Omega_c^*}{(w - i\gamma_{ge} - \delta)(w - \delta) - |\Omega_c|^2}$$

$$c_e(w) = \frac{\Omega_s(w - \delta)}{(w - i\gamma_{ge} - \delta)(w - \delta) - |\Omega_c|^2}.$$

The off-diagonal atomic polarization ρ_{eg} can thus be expressed as $\rho_{eg} = c_g^* c_e \simeq c_e$, while the normalized linear susceptibility function is $\bar{\chi}_s = \frac{\rho_{eg}}{\Omega_s}$ (see chapter 2). Redefining $(\delta - w) \rightarrow \nu$, we arrive at the expression for the normalized linear susceptibility $\bar{\chi}_s$ in Eq. 2.79 with

$$\bar{\chi}_s = \frac{\nu}{|\Omega_c|^2 - \nu^2 - i\gamma_{ge}\nu}. \quad (6.9)$$

The relationship between $\bar{\chi}_s$ and group velocity v_g (and transparency window) is explained in chapter 2 for an ideal Λ -level system. In section 6.10.1.3, we further illustrate the importance of optical pumping and polarization orientations of the control laser and the signal field for observing EIT in a Λ -level system comprised of multiple Zeeman sublevels.

6.10.1.2 The emergence of dark and bright states

The underlying principle for the cancellation of absorption in EIT is directly related to the phenomena of dark-state and coherent population trapping¹⁸³. Let us examine the effective Hamiltonian \hat{H}_{eff} with $\delta = 0$. In

^aWe note that the effective Hamiltonian \hat{H}_{eff} (Eq. 6.4) does not capture the repopulations of $\hat{\sigma}_{gg}$ and $\hat{\sigma}_{ss}$ due to spontaneous emissions ($-i\hbar\gamma_{ge}\hat{\sigma}_{ee}$). As a semi-classical analysis, we neglect the quantum jump processes^{164,165} and only consider the evolution of the stochastic wave-function $|\psi(t)\rangle$ under the effective Hamiltonian over time \tilde{t} . This approximation is valid in the quantum trajectory method for our initial condition $c_{gg} + c_{ss} \simeq 1$, as long as the jump probability is $p_{\text{jump}} = \langle \psi | \exp\left(\frac{i}{\hbar} \int_0^{\tilde{t}} dt (\hat{H}_{\text{eff}} - \hat{H}_{\text{eff}}^\dagger)\right) | \psi \rangle \simeq \int_0^{\tilde{t}} dt (\gamma_{ge}|c_{ee}|^2 + \gamma_{gs}|c_{ss}|^2) \ll 1$ for $\gamma_{gs} \simeq 0$.

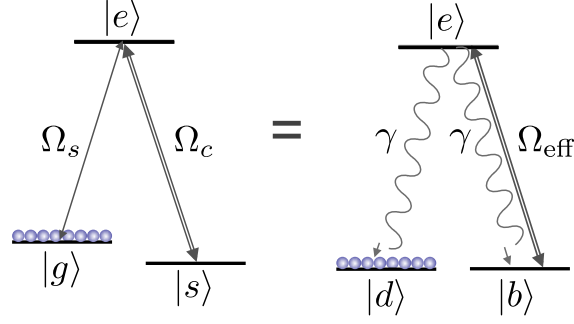


Figure 6.4: **Qualitative equivalence between electromagnetically induced transparency and coherent population trapping.** As shown by Eq. 6.10, the phenomena of EIT in the atomic bare-state basis can be equivalently described as a dark-state pumping process (CPT) in the dark- and bright-state basis for two-photon detuning $\delta = 0$.

the dark- and bright-state picture, we may equivalently write \hat{H}_{eff} (Eq. 6.4) in the following way,

$$\hat{H}_{\text{eff}}/\hbar = -i\gamma_{ge}\hat{\sigma}_{ee} - \Omega_{\text{eff}} \underbrace{(\sin^* \theta_d |g\rangle + \cos^* \theta_d |s\rangle)}_{|b\rangle} \langle e| - \Omega_{\text{eff}} |e\rangle \underbrace{(\sin \theta_d \langle g| + \cos \theta_d \langle s|)}_{\langle b|}, \quad (6.10)$$

where $\theta_d = \arctan(\Omega_s/\Omega_c)$ is the mixing angle, and $\Omega_{\text{eff}} = \sqrt{|\Omega_c|^2 + |\Omega_s|^2}$ is the effective Rabi frequency which couples the bright state $|b\rangle = \sin^* \theta_d |g\rangle + \cos^* \theta_d |s\rangle$ to the excited state $|e\rangle$. Similarly, we introduce a sibling, a dark state $|d\rangle = \cos^* \theta_d |g\rangle - \sin^* \theta_d |s\rangle$ (one of the three eigenstates of \hat{H}_{eff}) orthonormal to the bright state $|b\rangle$, which does not couple to the excited state $|e\rangle$ via \hat{H}_{eff} (thus, immune to spontaneous emission). Here, I used the notations, $\{\sin^* \theta_d, \cos^* \theta_d\}$, to define the complex conjugates of $\{\sin \theta_d, \cos \theta_d\}$.

In the picture of dark- and bright-state basis (Eq. 6.10), the atomic level diagram in the bare-state picture is transformed to a diagram akin to the case of optical pumping, as shown in Fig. 6.4. Here, the bright-state $|b\rangle$ couples dissipatively to the excited state $|e\rangle$ with an effective Rabi frequency Ω_{eff} , while the dark-state $|d\rangle$ is decoupled from the signal field \mathcal{E}_s and the control laser Ω_c . Thus, if the initial atomic state is prepared in an admixture of both ground states ($|g\rangle$ and $|s\rangle$), the coherently dressing Ω_{eff} will “optically pump” the atoms in the bright state $|b\rangle$ to the dark state $|d\rangle$ through the spontaneous emission from the excited state $|e\rangle$. As there are little atoms left in $|b\rangle$ after dark-state pumping (with negligible optical thickness for the $|b\rangle \leftrightarrow |e\rangle$ transition), the atoms will be trapped in the dark state via coherent population trapping (CPT) and the signal field will exhibit full spectroscopic transparency on resonance $\delta = 0$.

In the case of EIT, the initial atomic state can further be prepared to the dark state $|d\rangle \simeq |g\rangle$ (with $\Omega_s \ll \Omega_c$) prior to the EIT dressing (by means of optical pumping), from which excitations cannot occur. Therefore, by rotating the mixing angle $\theta_d = 0 \rightarrow \pi/4$, we can adiabatically transfer the initial state to a superposition state $|d\rangle = \frac{1}{2}(|g\rangle - |s\rangle)$ of maximum atomic coherence $\hat{\sigma}_{gs}$, as in stimulated Raman adiabatic transfer^{181,184} (STIRAP). There is a qualitative similarity between the adiabatic following of $|d\rangle$ and the dynamics of the dark-state polariton $\hat{\Psi}_d$. Heuristically considering the Fock state of the signal field, we can

write the dark state in a familiar form $|d\rangle = \cos^* \theta_d |\bar{g}_a, 1_s\rangle - \sin^* \theta_d |\bar{s}_a, 0_s\rangle$, identical to the single-excitation dark-state $|D, 1\rangle = \hat{\Psi}_d^\dagger |\bar{g}_a, 0_s\rangle$ (Eq. 2.69) in chapter 2. Hence, the quantum theory of dark-state polaritons⁸⁶ (chapter 2) is associated with the classical picture of dark- and bright-states in CPT and STIRAP.

6.10.1.3 Importance of the Zeeman sublevels

In the presence of multiple Zeeman sublevels, the susceptibility function $\chi_s = \frac{2g_d^2 N_A}{w_s} \bar{\chi}_s$ in Eq. 2.79 of chapter 2 and Eq. 6.9 generalizes to a normalized form $\bar{\chi}_s$ of

$$\bar{\chi}_s(\delta) = \frac{1}{N_c} \sum_{m_F} \frac{p_{m_F} |C_{m_F, \epsilon_s, m_F + \epsilon_s}^{F_g, 1, F_e}|^2 \delta}{|\Omega_c|^2 |C_{m_F + \epsilon_s - \epsilon_c, \epsilon_c, m_F + \epsilon_s}^{F_s, 1, F_e}|^2 - \delta^2 - i\gamma_g \delta}, \quad (6.11)$$

where $N_c = \sum_{m_F} p_{m_F} |C_{m_F, \epsilon_s, m_F + \epsilon_s}^{F_g, 1, F_e}|^2$ is the normalization constant, $\{\epsilon_s, \epsilon_c\}$ are the respective helicities for the signal field and the control lasers, and $C_{m_1, m_2, m_3}^{f_1, f_2, f_3} \equiv \langle f_1 m_1 f_2 m_2 | f_3 m_3 \rangle$ are the Clebsch-Gordan coefficients. In deriving Eq. 6.11, we assumed that the initial atomic state is $\hat{\rho}_a = \sum_{m_F} p_{m_F} |F_g, m_F\rangle \langle F_g, m_F|$.

For the ideal susceptibility function in Fig. 2.4 of chapter 2, the imaginary part of the susceptibility is $\text{Im}(\chi_s) = 0$ on resonance $\delta = 0$, thereby providing a transparency window for the signal field. At the same time, the real part of the linear susceptibility function $\text{Re}(\chi_s)$ provides a strong dispersion on resonance for slow-light propagation. In the presence of Zeeman populations p_{m_F} , however, the coherent atomic medium exhibits EIT only for specific polarization orientations $\{\epsilon_s, \epsilon_c\}$ of the signal field and the control lasers. Particularly, if the one of the Clebsch-Gordan coefficients $C_{m_F + \epsilon_s - \epsilon_c, \epsilon_c, m_F + \epsilon_s}^{F_g, 1, F_s}$ vanishes, the uncoupled Zeeman populations may have sufficient optical depths to cause dissipative absorption of the signal field and the absence of transparency.

As shown in Fig. 6.5, the EIT spectroscopy with lin//lin configuration (for the signal field and the control

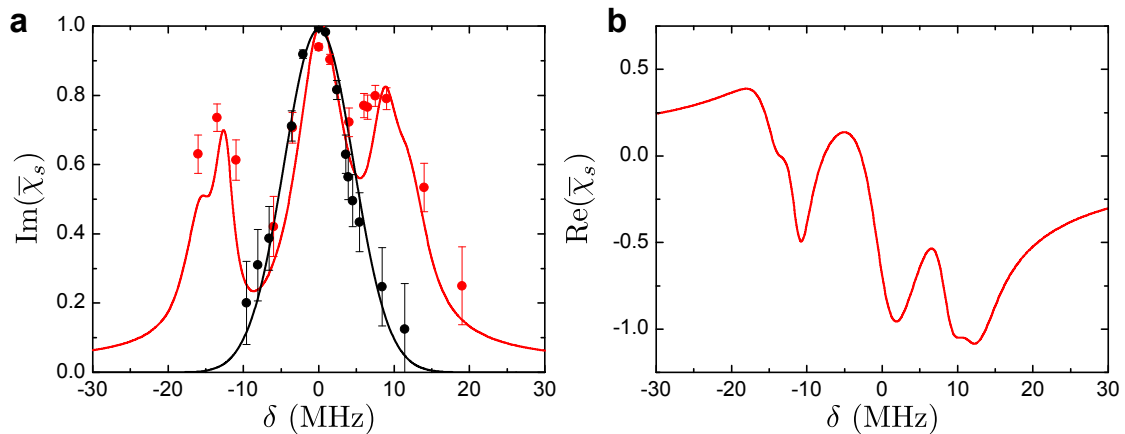


Figure 6.5: **EIT spectroscopy with lin//lin configuration.** **a**, Measurement of imaginary part of the susceptibility function $\text{Im}(\bar{\chi}_s)$. We show the measured $\text{Im}(\bar{\chi}_s)$ as red (black) points in the presence (absence) of control laser Ω_c with the polarization orientations given by $\epsilon_c = \epsilon_s = \hat{y}$. The data agrees well to the theoretically predicted spectra (lines). **b**, Theoretically predicted real part of the susceptibility function $\text{Re}(\bar{\chi}_s)$.

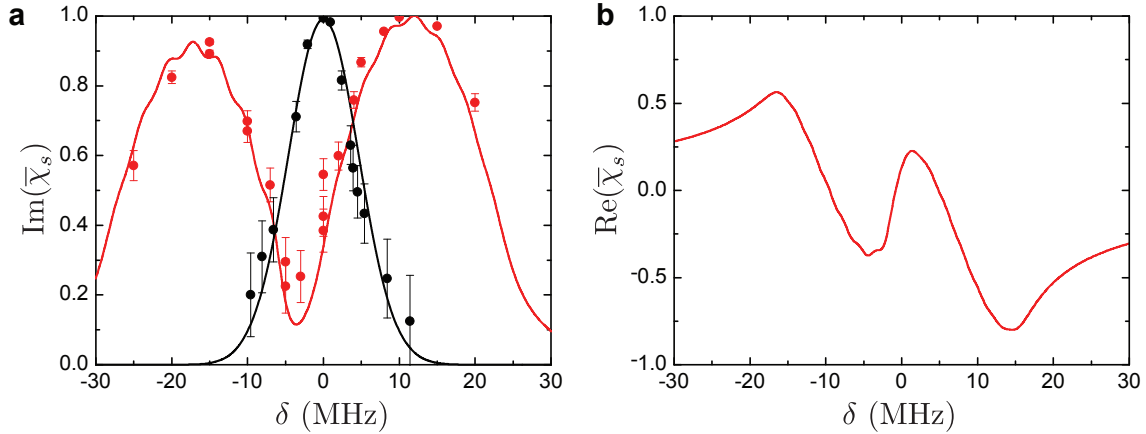


Figure 6.6: **EIT spectroscopy with $\sigma_{\pm}//\sigma_{\pm}$ configuration.** **a**, Measurement of imaginary part of the susceptibility function $\text{Im}(\bar{\chi}_s)$. We show the measured $\text{Im}(\bar{\chi}_s)$ as red (black) points in the presence (absence) of control lasers Ω_c with the polarization orientations given by $\epsilon_c = \epsilon_s = \sigma_{\pm}$. The data agrees well to the theoretically predicted spectra (lines). **b**, Theoretically predicted real part of the susceptibility function $\text{Re}(\bar{\chi}_s)$.

laser) does not show a transparency window on resonance. Since the two edge states ($|F' = 4, m_{F'} = \pm 4\rangle$) of the Zeeman sublevels in the electronically excited state $|e\rangle$ of $6P_{3/2}$ cannot couple to the hyperfine ground state $|s\rangle = |F = 3, m_F\rangle$ with the control laser Ω_c due to selection rule, the signal field experiences a strong resonant absorption by the optical depths for the residual atoms residing in the Zeeman sublevels $|F = 4, m_F = \pm 4\rangle$ of the hyperfine ground state $6S_{1/2}$ ($|g\rangle$) as represented by the peak in $\text{Im}(\bar{\chi}_s)$ around $\delta = 0$. The asymmetry in the two side peaks (Autler-Townes splitting for the Zeeman states coupled to the control laser) of Fig. 6.5 is due to the uncalibrated detuning Δ_c of the control laser respect to the $|s\rangle \leftrightarrow |e\rangle$

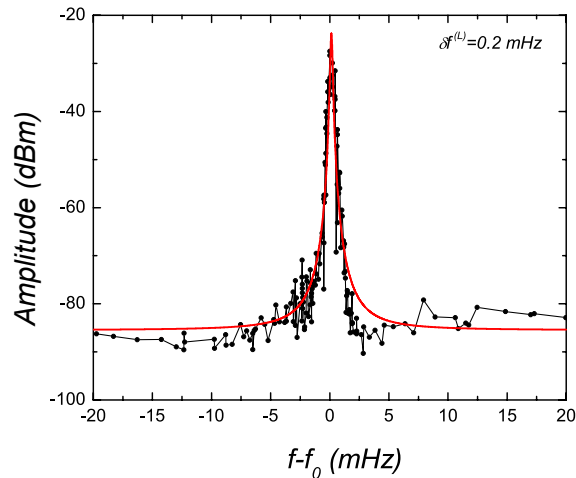


Figure 6.7: **Phase locked lasers for EIT spectroscopy.** We show the beat note spectrum between two lasers, responsible for the signal field and the control laser, in EIT spectroscopy. Assuming a Lorentzian spectrum, we deduce a beat-note linewidth of ~ 0.2 mHz, limited by the phase noise in the detection.

transition (which use as a fitting parameter in Fig. 6.5). The solid lines are the theoretical predictions based on Eq. 6.11, with the assumption of the initial state $p_{m_F} = 1/(2F_g + 1)$

Instead, we now apply a signal field and a control laser with helicities $\{\epsilon_s, \epsilon_c\} = \sigma_{\pm}$ in Fig. 6.6. As shown in Fig. 6.6a, the measured susceptibility function clearly demonstrates electromagnetically induced transparency around $\delta = 0$. Here, the red-detuned offset of the transparency window is due to the presence of the detuning Δ_c of the control laser. In Fig. 6.5b, we also show the real part of the linear susceptibility, similar to the result obtained for the ideal Λ -level system (Fig. 2.4). Furthermore, in our experiment³⁰ (Fig. 6.1), we initialize the atoms to a clock state $|g\rangle = |F = 4, m_F = 0\rangle$. With $\epsilon_{c,s} = \sigma_{\pm}$, the coherent dressings by the control and signal fields allow clock-state preserving transitions (section 6.6), which form a Λ -level with $|g\rangle = |F = 4, m_F = 0\rangle$, $|s\rangle = |F = 4, m_F = 0\rangle$, and $|e\rangle = |F' = 4, m_{F'} = \pm 1\rangle$. By optically pumping the ensemble to $|g\rangle = |F = 4, m_F = 0\rangle$ with efficiency $\sim 90\%$, we achieve a maximum transparency $T = 95\%$ on resonance.

6.10.2 Dynamic electromagnetically induced transparency

In chapter 2, we derived the Heisenberg-Langevin equations of motions in the polaritonic picture. In this section, we numerically solve the equations of motions and compare the theoretically simulated spatio-temporal modes \mathcal{E}_s to the experiment, where we store and retrieve a coherent state $|\alpha\rangle$ for various optical depths. We also show a theoretical simulation of time-reversal optimization of the storage and retrieval efficiency η_{sr} based on ref.¹⁸⁸ for our experimental parameters³⁰.

6.10.2.1 Scaling behavior to optical depth and pitfalls via dissipative absorption

As we discussed in chapter 2, the dynamics of the signal field $\hat{\mathcal{E}}_s(z, t)$ and the collective atomic excitation $\hat{S}(z, t)$ in the one-dimensional approximation is governed by the following coupled equations of motions (Eqs. 2.85–2.87),

$$(\partial_t + c\partial_z) \hat{\mathcal{E}}_s(z, t) = ig_d n_A(z) \frac{L}{\sqrt{N_A}} \hat{\mathcal{P}}(z, t) \quad (6.12)$$

$$\partial_t \hat{\mathcal{P}}(z, t) = -(\gamma_{ge} + i\Delta) \hat{\mathcal{P}}(z, t) + ig_d \sqrt{N_A} \hat{\mathcal{E}}_s(z, t) + i\Omega_c(z, t) \hat{S} + \sqrt{2\gamma_{ge}} \hat{F}_P \quad (6.13)$$

$$\partial_t \hat{S}(z, t) = -\gamma_{gs} \hat{S}(z, t) + i\Omega_c^*(z, t) \hat{\mathcal{P}} + \sqrt{2\gamma_{gs}} \hat{F}_S, \quad (6.14)$$

where $\hat{\mathcal{P}}(z, t)$ is the atomic polarization $|g\rangle - |e\rangle$ induced by the quantum field $\hat{\mathcal{E}}_s(z, t)$ in the presence of coherent dressing $\Omega_c(z, t)$. Assuming a coherent-state input, we numerically solve the complex-value equations of motions (Eqs. 6.12–6.14) by neglecting the Langevin terms $\hat{F}_S = \hat{F}_P = 0$, which do not contribute to normally-ordered expectation values. Here, we fit the atomic ensemble with a Gaussian spatial profile to infer the atomic density $n_A(z) = \frac{2N_A}{\sqrt{\pi}L} \exp(-4z^2/L^2)$ from the fluorescence measurement, and

the spatio-temporal mode of the control laser $\Omega_c(t - z/c)$ approximated by

$$\Omega_c(x) = \Omega_c \times \frac{\tanh [c_1 x] + \tanh [-c_2(x - \tau)]}{2}, \quad (6.15)$$

with the parameters $\{\Omega_c, c_1, c_2\}$ determined from independent measurements on the intensity of the control laser. N_A is determined from the measured value of the optical depth \tilde{d}_0 for the $|g\rangle - |e\rangle$ transition (optical depth is defined as the transmission $T = e^{-\tilde{d}_0}$ of the signal field absent the control laser). For the details of the derivations for Eqs. 6.12–6.14, I refer to the discussions in chapter 2.

Experimentally, we apply a control laser with $\Omega_c \simeq 24$ MHz (rise and fall times $\delta t_c = 1/c_1 = 1/c_2 \simeq 7$ ns, defined as the time-scales resulting in an intensity changes of 10%–90%) and a phase-locked signal laser \mathcal{E}_s (Fig. 6.7) resonant to $|g\rangle - |e\rangle$ transition (with two-photon detuning $\delta = 0$) in a counter-intuitive order¹⁸¹. The signal field \mathcal{E}_s is assumed to be in a coherent state $|\alpha\rangle$ with $|\alpha|^2 \simeq 0.3$ per pulse (Gaussian pulse width 30 ns for the incoming signal pulse). The relative delay between Ω_c and \mathcal{E}_s is tuned to maximize the storage and retrieval efficiency η_{sr} . As in the main experiment³⁰ (sections 6.1–6.9), we prepare the atomic ensemble into the clock state $|g\rangle = |F = 4, m_F = 0\rangle$ by optical pumping. We reduce the repetition rate of the laser cooling and trapping cycle from 40 Hz to 0.2 Hz in order to increase the atomic density^{242,243} via compressed MOT (CMOT)²⁴³ for 200 ms after the normal MOT loading and cooling (4 s). We then further cool the atoms with polarization gradient cooling for 50 ms, followed by optical pumping (1 ms) to the clock state. With

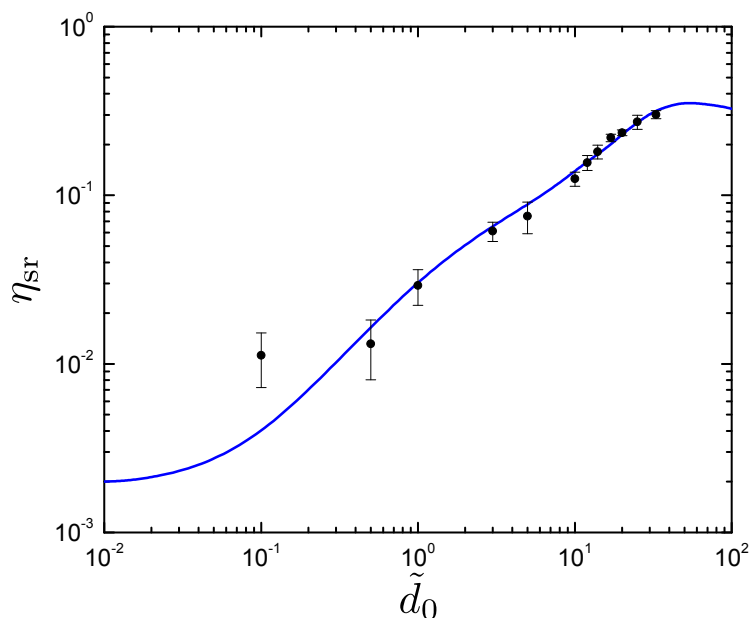


Figure 6.8: **Investigation of reversible transfer of a coherent state to and from an atomic memory.** We study the dependence of storage and retrieval efficiency η_{sr} to the optical depth \tilde{d}_0 , with the measurements shown by black points. We achieve a maximum efficiency of $\eta_{sr} \simeq 30\%$ at $\tilde{d}_0 \simeq 33$. The theoretical simulation (blue line) based on Eqs. 6.12–6.14 shows excellent agreement with our measurement. The error bars indicate the statistical uncertainty of 1 s.d.

the improved setup, we achieve a maximum resonant optical depth of $\tilde{d}_0 \gtrsim 50$, albeit with reduced optical pumping efficiency $\sim 70\%$ due to radiation trapping, compared to the main experiment³⁰ (sections 6.1–6.9). The optical depth \tilde{d}_0 is varied by tuning the value of the magnetic field to the desired value during the normal MOT phase (before compression).

In Fig. 6.8, we show the overall transfer efficiency η_{sr} for storing and retrieving a coherent state $|\alpha\rangle$ in an atomic ensemble (with storage time $\tau = 1 \mu\text{s}$) as a function of optical depth \tilde{d}_0 (see e.g., Fig. 2.6 for a time-domain measurement at $\tilde{d}_0 = 20$). In particular, we achieve a maximum storage and retrieval efficiency of $\eta_{\text{sr}} = 30 \pm 2 \%$ at optical depth $\tilde{d}_0 \simeq 33$. We also find excellent agreement between the theoretical predicted EIT efficiency $\eta_{\text{sr}}^{\text{theory}}(\tilde{d}_0)$ and the experimentally measured η_{sr} . We emphasize that for higher optical depth $\tilde{d}_0 \gtrsim 60$ (a region beyond the capability at the time), the storage and retrieval efficiency η_{sr} is expected to decrease, due to the reduced bandwidth of the EIT medium at high \tilde{d}_0 (chapter 2, see also Fig. 6.10). For further improvement in η_{sr} , it is thus important to increase the intensity of the control laser^b for higher \tilde{d}_0 .

In order to optimize η_{sr} for a finite \tilde{d}_0 , we need to compromise the control laser's intensity between two competing regimes. On the one hand, (1) a large Rabi frequency Ω_c is preferred to increase bandwidth of the EIT medium and to avoid dissipative absorption of \mathcal{E}_s . On the other hand, (2) a sufficiently small Ω_c is required to compress the signal field's wavepacket inside the ensemble for avoiding significant leakage. In analogy, these two competing effects^c at finite \tilde{d}_0 can be cast in terms of the proper shaping of the spatio-temporal mode of the signal field \mathcal{E}_s for a fixed Ω_c . In the next section, we discuss an iterative optimization strategy based on the works by Gorshkov *et al.*^{187–189}, which leads to global maximization of η_{sr} in the fully adiabatic regime, as demonstrated experimentally by Novikova *et al.*²³⁵.

6.10.2.2 Iterative optimization strategy based on time-reversal symmetry

In the fully adiabatic regime, the mapping process is well described by the dynamics of dark-state polariton $\hat{\Psi}_d(z, t) = \cos \theta_d(t) \hat{\mathcal{E}}_s(z, t) - \sin \theta_d(t) \hat{\mathcal{S}}(z, t)$ with a beamsplitter-like Hamiltonian $\hat{H}_{\text{int}}^{(\text{map})}$ (Eq. 2.84) in chapter 2, given by

$$\hat{H}_{\text{int}}^{(\text{map})} = i\dot{\theta}_d(z, t) \left(\hat{\mathcal{E}}_s(z, t) \hat{\mathcal{S}}^\dagger(z, t) - \hat{\mathcal{E}}_s^\dagger(z, t) \hat{\mathcal{S}}(z, t) \right). \quad (6.16)$$

$\dot{\theta}_d(z, t)$ gives the rate of change in the mixing angle $\theta_d(z, t)$, which we assume to be small in order for adiabatic passage (chapter 2). The unitary transformation $\hat{U}_{\text{int}}^{(\text{map})}(t) = \exp\left(-\frac{i}{L\hbar} \int_0^t dt' \int_0^L dz \hat{H}_{\text{int}}^{(\text{map})}(z, t')\right)$

^bWith a large Rabi frequency Ω_c for the control laser, there may be a non-negligible contribution from a competing four-wave mixing process²⁴⁴, where the atoms initially at $|g\rangle$ is off-resonantly driven to $|s\rangle$ by Ω_c generating an anti-Stokes photon, followed by a resonant scattering back to $|g\rangle$ with Ω_c seeded by the signal field (Stokes photon). We do not consider this four-wave mixing process in our calculation, as it is suppressed by the large ground-state splitting ~ 9 GHz.

^cFor a given Ω_c , we need to keep the signal pulse \mathcal{E}_s as short as possible to compress \mathcal{E}_s within the atomic sample and to avoid leakage. On the other hand, we need to broaden the spatial extent of \mathcal{E}_s as much as possible to reduce its pulse bandwidth well below the EIT bandwidth of the coherent atomic medium.

describes the mapping process, where we individually define the storage (η_s) and retrieval (η_r) efficiencies as

$$\eta_s = \frac{\int dz \langle \hat{\mathcal{S}}^\dagger(z, t_s) \hat{\mathcal{S}}(z, t_s) \rangle}{\int dz \langle \hat{\mathcal{E}}_s^\dagger(z, t_0) \hat{\mathcal{E}}_s(z, t_0) \rangle} \quad (6.17)$$

$$\eta_r = \frac{\int dz \langle \hat{\mathcal{E}}_s^\dagger(z, t_f) \hat{\mathcal{E}}_s(z, t_f) \rangle}{\int dz \langle \hat{\mathcal{S}}^\dagger(z, t_r) \hat{\mathcal{S}}(z, t_r) \rangle}, \quad (6.18)$$

evaluated at the respective times t_s (falling edge) and t_r (rising edge) with delay $\tau = t_r - t_s$. $\hat{\mathcal{E}}_s(z, t_0)$ and $\hat{\mathcal{E}}_s(z, t_f)$ give the initial (incoming) and final (outgoing) states of the signal field.

Qualitatively, it is easier to understand the optimal retrieval strategy for η_r than to understand the optimal storage η_s , as we assume a pre-existing collective spin-wave with a profile $\langle \hat{\mathcal{S}}^\dagger(z, t_r) \hat{\mathcal{S}}(z, t_r) \rangle$ at time t_r . In this case, unlike the storage, we are not restrained by the control laser due to the leakage of the signal field. In practice, however, an abrupt activation of $\Omega_c(z, t)$ can reduce the retrieval efficiency by the non-adiabatic transition of $\Psi_d(z, t)$ to the bright-state polariton $\Psi_b(z, t)$. Here, we give a heuristic argument for the optimal η_r^{opt} (ref. 188), where we assume a fully adiabatic regime for $\Omega_c(z, t)$ and an optimally shaped $\langle \hat{\mathcal{S}}^\dagger(z, t_r) \hat{\mathcal{S}}(z, t_r) \rangle$. For a rigorous proof in the adiabatic regime, I refer to the original works in refs. 187–189. We then show that the time-reversed version of the optimal retrieval process leads to an optimal storage with efficiency $\eta_s^{\text{opt}} = \eta_r^{\text{opt}}$.

We first consider the forward retrieval in a Gaussian signal mode with beam-waist w_0 (section 2.3.2.2). Beyond the Rayleigh range, the solid-angle Ω_{solid} of this mode is given by $\Omega_{\text{solid}} \simeq \frac{\lambda^2}{4\pi w_0^2 \ln 2}$. The collectively enhanced scattering rate into this mode is then simply $\Gamma_c = \Omega_{\text{solid}} N_A^2 \Gamma_0 = \frac{\lambda^2}{4\pi w_0^2 \ln 2} N_A^2 \Gamma_0$, whereas the scattering rate into all other modes is given approximately by $\Gamma_n \simeq N_A \Gamma_0$. Here, $\Gamma_0 = 2\pi\gamma_{ge}$ is the single-atom scattering rate. The optimal retrieval efficiency η_r^{opt} is then given by

$$\eta_r^{\text{opt}} = \frac{\Gamma_c}{\Gamma_c + \Gamma_n} \simeq \frac{3\tilde{d}_0}{3\tilde{d}_0 + 8} \simeq 1 - \frac{8}{3\tilde{d}_0}, \quad (6.19)$$

where we used the relations for resonant absorption cross-section $\sigma_0 = 3\lambda^2/2\pi$ and optical depth $\tilde{d}_0 \simeq N_A \sigma_0 / (\pi w_0^2)$. Thus, we find that the optimal retrieval efficiency for η_r^{opt} depends only on the optical depth $\tilde{d}_0 = \frac{g_a^2 N_A}{\gamma_{ge} \kappa_{\text{eff}}}$ (where $\kappa_{\text{eff}} = c/L$), which plays the role of a cooperativity parameter (chapter 2).

From the qualitative argument given above for achieving the optimal η_r^{opt} , we now discuss the principle of time-reversal as an optimization tool for storage η_s . We consider the storage map $\hat{U}_{\text{int}}^{(\text{map})}(t)$ on the initial state $|\bar{g}_a, 1_s\rangle$ given by $|D, 1\rangle = \hat{\Psi}_d^\dagger |\bar{g}_a, 0_s\rangle$ in the Schrödinger picture. The storage probability η_s is then given by

$$\eta_s^{\text{opt}} = |\langle \bar{s}_a, 0_s | \hat{U}_{\text{int}}^{(\text{map})}(t) | \bar{g}_a, 1_s \rangle|^2. \quad (6.20)$$

Using the unitarity relation for $\hat{U}_{\text{int}}^{(\text{map})\dagger}(t) = \hat{U}_{\text{int}}^{(\text{map})}(-t)$, we find that the storage efficiency is identical to the retrieval efficiency,

$$\eta_s^{\text{opt}} = |\langle \bar{g}_a, 1_s | \hat{U}_{\text{int}}^{(\text{map})}(-t) | \bar{s}_a, 0_s \rangle|^2 = \eta_r^{\text{opt}}, \quad (6.21)$$

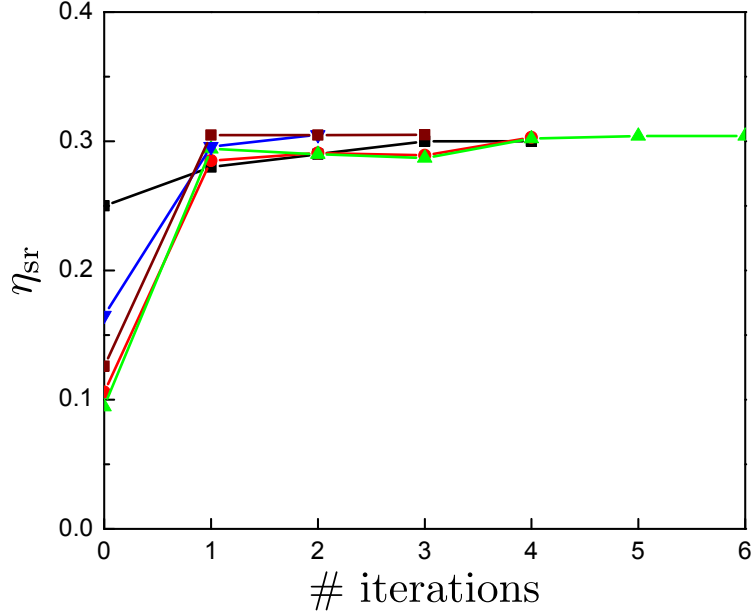


Figure 6.9: **Iterative optimization scheme for maximizing storage and retrieval efficiency.** We apply theoretically the time-reversal symmetry¹⁸⁶ for optimizing the EIT efficiency η_{sr} at optical depth $\tilde{d}_0 = 17$, where η_{sr} converges to $\simeq 30\%$ after 2 – 3 steps. The various colors indicate different initial conditions for the signal fields $\mathcal{E}_{s,in}^{(1)}(z, t)$.

if the time-reversed version $\hat{U}_{int}^{(map)}(t)$ of the retrieval map $\hat{U}_{int}^{(map)}(-t)$ is used for storage.

This means that if the retrieval map $\hat{U}_{int}^{(map)}(-t)$ yields an optimal retrieval η_r^{opt} of some spin-wave mode $\tilde{S}(z, t)$ to an output signal mode $\tilde{\mathcal{E}}_s(z, t)$, we can realize an inverse evolution by time-reversing $\hat{U}_{int}^{(map)}(t)$ (time-reversing the control $\Omega_c(-z, t)$ and the signal fields $\tilde{\mathcal{E}}_s(-z, t)$ in Eq. 6.16) to achieve optimal efficiency $\eta_s^{opt} = \eta_r^{opt}$, where the incoming field $\tilde{\mathcal{E}}_s(-z, t)$ is mapped onto the stationary excitation $\tilde{S}(z, t)$. Here, we note that the negative sign in z implies a backward propagation, corresponding to the situation of backward storage ($\tilde{\mathcal{E}}_s(-z, t), \Omega_c(-z, t)$) followed by forward retrieval ($\tilde{\mathcal{E}}_s(-z, t), \Omega_c(-z, t)$). The time-reversal symmetry also applies to forward storage followed by forward retrieval, as in our experimental setup³⁰, albeit with reduced optimal efficiency $\eta_r^{opt} = \eta_s^{opt} \sim 1 - \frac{1}{\sqrt{\tilde{d}_0}}$ (ref.¹⁸⁶). For a rigorous proof of time-reversal symmetry as an optimization tool, I refer to ref.¹⁸⁸ where Eqs. 6.12–6.14 are analytically solved in the fully adiabatic regime.

In the non-adiabatic regime, as in our case, the time-reversal optimization generally does not converge to the global maximum of η_{sr} . Such a ‘fast’ storage regime has been considered in ref.²⁴⁵ using gradient ascent methods. Nonetheless, we numerically apply the method of time-reversal symmetry to theoretically maximize η_{sr}^{opt} for a given optical depth \tilde{d}_0 . We start by storing an initial signal field $\mathcal{E}_{s,in}^{(1)}(z, t)$ and retrieving to $\mathcal{E}_{s,out}^{(1)}(z, t)$ in step $i = 1$. We then apply the time-reversed version of the output $\mathcal{E}_{s,out}^{(1)}(z, t)$ in step $i = 1$ into the input signal field $\mathcal{E}_{s,in}^{(2)}(z, t) = \mathcal{E}_{s,out}^{(1)}(-z, t)$ in step $i = 2$. By iterating this process $i \rightarrow n$ until $\mathcal{E}_{s,in}^{(n)}(z, t) = \mathcal{E}_{s,in}^{(n)}(-z, t)$, we optimize the storage and retrieval efficiency η_{sr}^{opt} . Fig. 6.9 shows such a

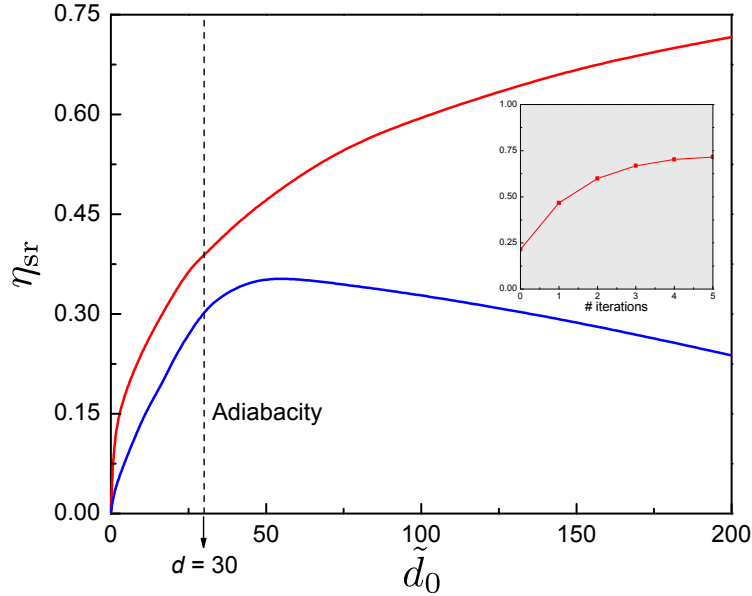


Figure 6.10: **Time-reversal optimization of EIT transfer efficiency.** We show the transfer efficiency η_{sr} as a function of optical depth \tilde{d}_0 . We also compare the result of the optimal η_{sr}^{opt} (red line) to η_{sr} (blue line) given for our experimental parameters in Fig. 6.8.

numerical process for optical depth $\tilde{d}_0 = 17$ (with same parameters $\{c_1, c_2, \Omega_c\}$ used in section 6.10.2.1) starting from various initial conditions $\mathcal{E}_{s,in}^{(1)}(z, t)$, where we converge to the same maximum EIT efficiency $\eta_{sr}^{opt} \simeq 30\%$ after 2 – 3 iterations.

In addition, this numerical optimization scheme allows us to benchmark the maximum transfer efficiency $\tilde{\lambda} \simeq \eta_{sr}^{opt}$ of entanglement as a function \tilde{d}_0 . In Fig. 6.10, we apply the time-reversal optimization as a function of optical depth \tilde{d}_0 , shown as red line. We demonstrate that η_{sr}^{opt} (red line) can be further improved relative to the EIT efficiency η_{sr} of our experiment parameters (blue line) (see also Fig. 6.8) beyond $\tilde{d}_0 \gtrsim 50$. In particular, unlike Fig. 6.8, we find a monotonic improvement in the transfer efficiency η_{sr} as a function of optical depth \tilde{d}_0 . For reference, we indicate the boundary at which the adiabatic condition $\tilde{d}_0 \gamma_{ge} \delta t_c \gg 1$ is met⁸⁷.